nature portfolio

https://doi.org/10.1038/s41586-021-04344-y

Supplementary information

Differential clock comparisons with a multiplexed optical lattice clock

In the format provided by the authors and unedited

Supplementary Information: Differential clock comparisons with a multiplexed optical lattice clock

Xin Zheng, Jonathan Dolde, Varun Lochab, Brett N. Merriman, Haoran Li, Shimon Kolkowitz*

University of Wisconsin-Madison

CONTENTS

*To whom correspondence should be addressed. E-mail: kolkowitz@wisc.edu

A. Balanced trap depths of symmetrically prepared ensembles

To verify that the ensemble pairs are symmetrically prepared relative to the lattice beam waist and have consistent atomic temperatures, we perform motional sideband spectroscopy on the ${}^1S_0 \leftrightarrow {}^3P_0$ (denoted as $|g\rangle \leftrightarrow |e\rangle$ below) transition with 150 ms pulse at 689 nm. (Fig.S1). The red (blue) detuned sideband corresponds to the transition from $|g, n_g\rangle \leftrightarrow |e, n_e = n_g - 1\rangle$ ($|g, n_g\rangle \leftrightarrow |e, n_e = n_g + 1\rangle$), where $n_{g/e}$ is the vibrational quantum number in the ground/excited state. The lattice trap depth is determined by the cut-off frequency of the sidebands [1] and the axial temperature is extracted using the ratio of the area under the blue and red detuned sidebands. The lattice alignment is optimized such that the trapping frequencies between the two ensembles agree to within the 1-kHz sampling interval, equivalent to a differential lattice trap depth below 1 E_{rec}. The temperatures of the two ensembles agree to within 0.1 μK, inferred by the axial temperature (0.7 μK and mean quantum occupation number of 0.15) extracted from the motional sidebands. The radial temperature (0.6 μK) is determined by probing the Doppler broadened profile with a separate clock beam path perpendicular to the optical lattice.

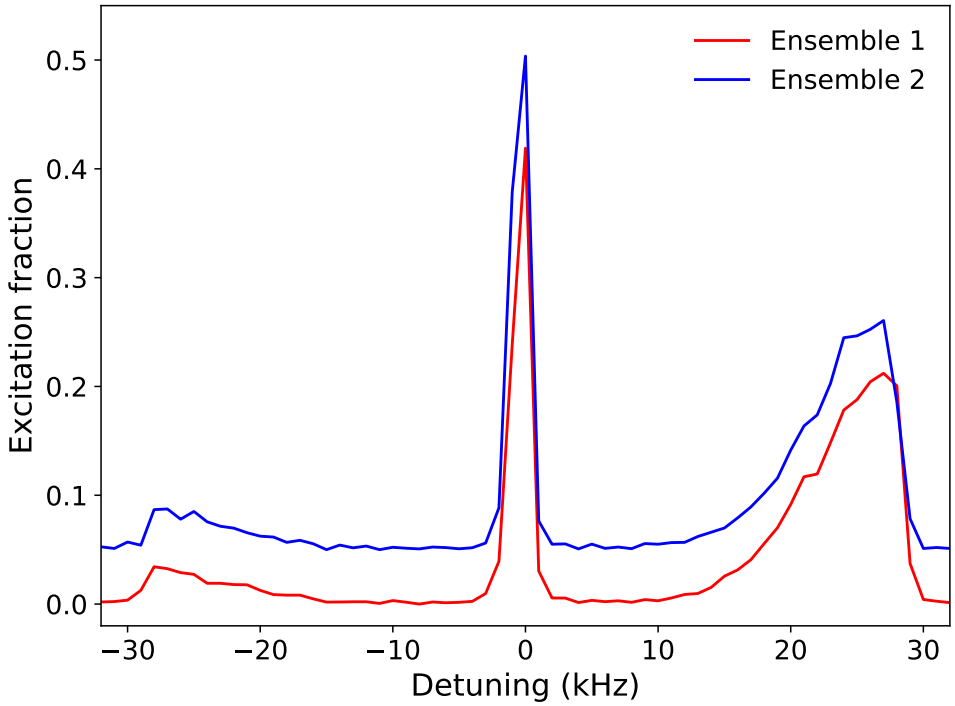

FIG. S 1. Motional sideband spectroscopy for two ensembles separated by 1 cm with trap depth of 20 E_{rec}. This is taken with a 150 ms pulse on the ${}^1S_0 \leftrightarrow {}^3P_0$ clock transition. The fitted sidebands give the mean vibrational quantum state occupation number and axial temperature, and are consistent for both ensembles within the 1-kHz resolution. The excitation fractions of ensemble 2 (blue) is shifted up by +0.05 along the y-axis for clarity.

B. Raman scattering, lifetime and lattice trap depth dependent contrast

To reduce the off-resonant lattice photon induced Raman scattering [2], we would prefer to operate at shallower lattice trap depths. However, while gravity creates an energy difference between adjacent lattice sites and suppresses tunneling for vertical one-dimensional lattices, we observe reduced lifetimes for both the ground and excited state atoms at shallow trap depths

($< 15\ E_{\rm rec}$), likely due to residual parametric heating from the lattice. At deeper trap depths ($> 30\ E_{\rm rec}$), the lifetimes for atoms in the excited state are reduced to below 15 seconds, likely limited by Raman scattering from the lattice light. Furthermore, we also observe decreased lifetimes in the ground state atoms at much deeper lattice trap depths, suggesting lattice-intensity-dependent heating.

The measured contrasts for synchronous Ramsey interrogation for both ensembles prepared with approximately 2400 atoms drops from 0.6 to 0.2 as the lattice trap depth is increased from 20 $E_{\rm rec}$ to 45 $E_{\rm rec}$ (Fig.S2). This is likely due to a combination of Raman scattering, which scales linearly to lattice trap depth U, and p-wave collision induced density shift, which scales as $U^{5/4}$ [3]. The competition between reduced lifetime, reduced atom number as well as increased contrast when lowering the lattice trap depth leads to lattice trap depths between 15 to 20 $E_{\rm rec}$ for optimal interrogation sensitivity under our current operating conditions. For all data taken in this paper, we operate at a lattice depth of 20 $E_{\rm rec}$ during clock interrogation, unless otherwise specified. For a synchronous Ramsey interrogation time of 8 s, approximately the same interrogation time as the data shown in Fig.3b in the main text, we measure a contrast of 0.65 at the operational trap depth of 20 $E_{\rm rec}$.

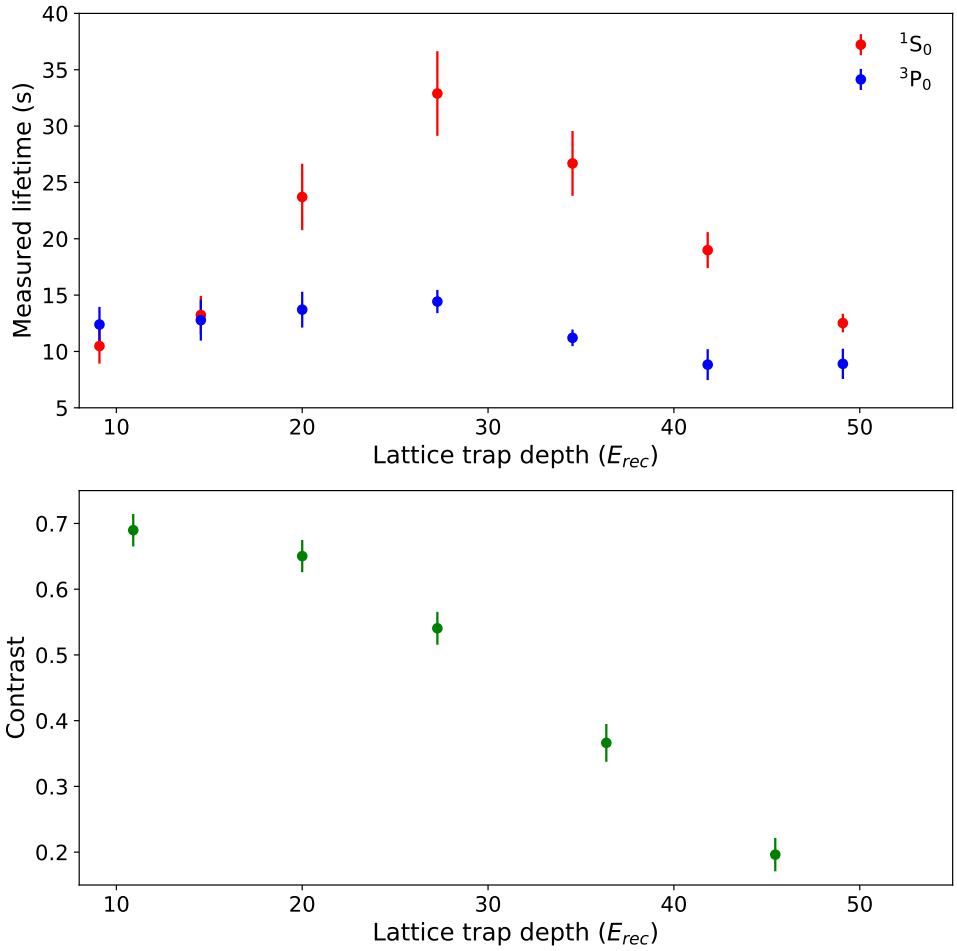

FIG. S 2. Top: Measurement of ground (red) and excited (blue) state atom lifetimes as a function of lattice trap depth. Bottom: Measurement of synchronous Ramsey contrast at 8 s interrogation time and approximately 2400 atoms per ensemble at different lattice trap depths.

C. Operational magic wavelength

The ac Stark shift at a particular lattice trap depth U_0 for π-transition ($\Delta m_F = 0$) starting from the ground state $|g, m_F\rangle$ can be expressed as [4, 5]

$$\Delta\nu_{\rm ac} = \Big(\Delta\kappa^S + \Delta\kappa^V m_F \xi \hat{\epsilon}_k \cdot \hat{\epsilon}_B + \Delta\kappa^T (3\cos^2\theta - 1)\big[3m_F^2 - F(F+1)\big]\Big) U_0, \tag{1}$$

where $\Delta\kappa^{S,V,T}$ are the differential scalar, vector, and tensor shift coefficients between excited and ground states, respectively; ξ is the lattice light ellipticity; $\hat{\epsilon}_{k,B}$ are units vectors along the lattice beam wave vector and magnetic field quantization axis, respectively; θ is the angle between the (nearly) linear lattice polarization and $\hat{\epsilon}_B$.

Similarly, the ac Stark shift for $\sigma^{\pm}$-transition ($\Delta m_F = \pm 1$) starting from $|g, m_F\rangle$ has the form

$$\begin{aligned}\Delta\nu_{\rm ac} = \Big(&\Delta\kappa^S + \big(\kappa_e^V (m_F \pm 1) - \kappa_g^V m_F\big)\xi\hat{\epsilon}_k \cdot \hat{\epsilon}_B \\ &+ \Delta\kappa^T (3\cos^2\theta - 1)\big[-F(F+1)\big] \\ &+ (3\cos^2\theta - 1)\big[\kappa_e^T (3m_F \pm 1)^2 - \kappa_g^T 3m_F^2\big]\Big) U_0,\end{aligned} \tag{2}$$

where $\kappa_g^{V,T}$ ($\kappa_e^{V,T}$) are vector, tensor coefficients for ground (excited) states, respectively. We note that the multi-polarizability and hyperpolarizability are neglected in this model [3, 6, 7].

An operational magic wavelength corresponds to the lattice frequency where the scalar and tensor Stark shifts cancel, and the remaining vector Stark shift can be eliminated by both using a linearly polarized lattice beam ($\xi \approx 0$) and averaging between the $|\pm m_F\rangle$ state manifolds.

In this work, the operational magic wavelength is chosen to be 368 554.4849(1) GHz for $|g, \pm 9/2\rangle \leftrightarrow |e, \pm 9/2\rangle$ (π transition) as given by the previous work [8]. However, the above wavelength no longer works for the $|g, \pm 5/2\rangle \leftrightarrow |e, \pm 3/2\rangle$ transition because of m_F dependence in the tensor Stark shift. In the limit where the lattice frequency is near the magic wavelength, we have $\Delta\kappa^T = \kappa_e^T - \kappa_g^T \simeq \kappa_e^T = -0.0058(23)$ mHz/$E_{\rm rec}$ [5]. We then would expect a differential shift of $-117\ \Delta\kappa^T U_0$ for the $|g, \pm 5/2\rangle \leftrightarrow |e, \pm 3/2\rangle$ transition using the above operational magic wavelength and assuming $\theta \approx 0$. At a typical lattice trap depth of $U_0 = 20\ E_{\rm rec}$, this corresponds to a shift of about +13.5 mHz.

To find the operational magic wavelength for the $|g, \pm 5/2\rangle \leftrightarrow |e, \pm 3/2\rangle$ transition, the lattice frequency is scanned across a range of $\pm$800 MHz and the contrasts of synchronous Ramsey interrogation are measured at each lattice detuning (main text Fig.2**e**). The optimal contrast is found at lattice frequency of 368 554.810(30) GHz, which is blue shifted by +325(30) MHz compared to the operational magic wavelength for the $|g, \pm 9/2\rangle \leftrightarrow |e, \pm 9/2\rangle$ transition.

D. Differential Zeeman shifts and magnetic field sensitivities

For the ${}^1S_0 \leftrightarrow {}^3P_0$ clock transition, the linear Zeeman shift at a magnetic field B for the π-transition starting from ground state $|g, m_F\rangle$ can be written as [9]

$$\Delta\nu_{L,\pi} = -\delta g m_F \mu_0 B, \tag{3}$$

where δg is the differential Landé g-factor between the ground and excited states, $\mu_0 = \mu_B/h$, where μ_B is the Bohr magneton and h is the Planck constant.

Similarly, we can express the linear Zeeman shift for $\sigma^{\pm}$ transition from the ground state $|g, m_F\rangle$ as

$$\Delta\nu_{L,\sigma^{\pm}} = -(\pm g_I + \delta g(m_F \pm 1))\mu_0 B, \tag{4}$$

where g_I is the nuclear Landé g-factor.

With $\delta g \mu_0 = -108.4$ Hz/G and $g_I \mu_0 = -185$ Hz/G as input [9], we would expect the linear Zeeman shift coefficient for the $|g, \pm 9/2\rangle \leftrightarrow |e, \pm 9/2\rangle$ π-transition to be

$$\mu_L^{\pm 9/2 \leftrightarrow \pm 9/2, \pi} = \pm 487.8 \text{ Hz/G} \tag{5}$$

Similarly for the $|g, \mp 5/2\rangle \leftrightarrow |e, \mp 3/2\rangle$ $\sigma^{\pm}$-transition

$$\mu_L^{\mp 5/2 \leftrightarrow \mp 3/2, \sigma^{\pm}} = \pm 22.4 \text{ Hz/G}, \tag{6}$$

which is a factor of 22 smaller in the magnetic field sensitivity compared to the $|g, \pm 9/2\rangle \leftrightarrow |e, \pm 9/2\rangle$ transition.

The quadratic Zeeman shift has negligible m_F dependence and can be written as

$$\Delta \nu_Q = \delta_B^{(2)} \mu_0 B^2, \tag{7}$$

where $\delta_B^{(2)} \mu_0 = -0.233(5)$ Hz/G^2 is the quadratic Zeeman shift coefficient.

Under a typical bias magnetic field of 2 G and a magnetic field gradient of 15 mG/cm, the differential linear Zeeman shift (for the $|g, +5/2\rangle \leftrightarrow |e, +3/2\rangle$ transition) between two ensembles separated by 1 cm is approximately 350 mHz, and the differential quadratic Zeeman shift is approximately 14 mHz.

E. Ellipse fitting

In order to extract the differential frequency detuning between the two ensembles we interrogate, we follow the procedure demonstrated by [10, 11]. After a Ramsey interrogation time T, the excitation fraction of each ensemble can be expressed as

$$P_1 = \frac{1}{2}\Big(1 + C_1\big[\cos(\omega_1 - \omega_l)T\big]\Big), \tag{8}$$

$$P_2 = \frac{1}{2}\Big(1 + C_2 \cos\big[(\omega_1 + \omega_d - \omega_l)T\big]\Big), \tag{9}$$

where C_i is the contrast for ensemble i, ω_1 is the clock transition frequency of ensemble 1, ω_l is the frequency of the laser, and ω_d is the clock transition frequency difference between ensemble 2 and 1. We can then re-express these excitation fractions as functions of angles θ and ϕ, where θ is the atom-laser phase, $(\omega_1 - \omega_l)T$, and ϕ is the differential phase between the ensembles, $\omega_d T$.

$$P_1 = \frac{1}{2}\Big(1 + C_1 \cos(\theta)\Big), \tag{10}$$

$$P_2 = \frac{1}{2}\Big(1 + C_2 \cos(\theta + \phi)\Big). \tag{11}$$

Since we are operating at Ramsey interrogation times well beyond the laser coherence time, θ is effectively random and uniformly distributed from 0 to 2π, while ϕ should stay constant across experimental shots with the same Ramsey interrogation time.

In order to extract ϕ from our data, we plot the excitation fraction in each ensemble for a given experimental shot as a single point on a parametric plot, with ensemble 2 on the vertical axis and ensemble 1 on the horizontal axis. As shots build up, an ellipse is traced out, with points randomly sampling the perimeter of the ellipse due to the random distribution of θ. We then fit to this ellipse using least-squares approach [12] and extract $\phi = 2\arctan(b/a)$, where a and b are the fitted semi-major and semi-minor axis, respectively.

1. Phase extraction variance and biased error

In order to accurately determine our uncertainty in extracting ϕ, we calculate the variance of ϕ through the variance in P_1 and P_2 due to QPN. For convenience, we can define (assuming $C_1 = C_2 = C$)

$$x = \frac{C}{2}\cos(\theta), \tag{12}$$

$$y = \frac{C}{2}\cos(\theta + \phi), \tag{13}$$

such that we can express the variance of ϕ as

$$\sigma^2(\phi) = \left|\frac{\partial\phi}{\partial x}\right|^2 \sigma^2(x) + \left|\frac{\partial\phi}{\partial y}\right|^2 \sigma^2(y), \tag{14}$$

The partial derivatives can be evaluated through Jacobian matrix inversion, and the variance in x and y due to quantum projection noise (QPN) can be expressed as

$$\sigma^2(x) = \frac{1}{N_1}P_1(1 - P_1), \tag{15}$$

$$\sigma^2(y) = \frac{1}{N_2}P_2(1 - P_2), \tag{16}$$

which gives a expression for the variance of ϕ

$$\sigma^2(\phi) = \frac{4}{C^2}\left(\csc^2(\theta)\sigma^2(x) + \csc^2(\theta + \phi)\sigma^2(y)\right) \tag{17}$$

Finally, since we take repeated measurements of ϕ for a random θ, we average over a uniform θ distribution to get an average variance in ϕ as the following.

$$\langle\sigma^2(\phi)\rangle = \frac{4}{C^2}\left(\int_0^{2\pi}\frac{d\theta}{2\pi}\frac{1}{\csc^2(\theta)\sigma^2(x) + \csc^2(\theta + \phi)\sigma^2(y)}\right)^{-1} \tag{18}$$

In the case where $C = 1$, QPN results in a variance of $\langle\sigma^2(\phi)\rangle = 2/(NC^2)$, which is the familiar result for QPN-limited Ramsey spectroscopy. For $C < 1$, Var(ϕ) is scaled by a factor depending on the phase and contrast (Fig.S3). Counterintuitively, the QPN limit is minimized at $\phi \approx 0$ or π (a line) where the fits are most biased and the QPN limit is maximized at $\pi/2$ (a circle) where the fits are least biased. This would suggest operating at a ϕ closer to 0 or π to push the QPN limit lower, while ensuring accurate characterization and correction of fitting errors due to higher bias at that operational ϕ. This can be accomplished by running Monte-Carlo simulations with known phases and experimental parameters as input, allowing us to bound the biased error in ellipse fitting below 3% at $\phi \approx 0.44$ rad with 2400 atoms in each ensemble (Fig.S4).

2. Determination of Ramsey contrast

We determine the Ramsey contrast independently for each ensemble, rather than extracting it from the fitted ellipse. To do so, we plot the histogram of the excitation fractions of each ensemble, revealing a bimodal distribution. The contrast is then straightforwardly extracted by taking the difference of the two local maxima. This is then corrected for by adding a small offset based on the Monte-Carlo simulations with known contrasts and QPN as input. Fig.S5a

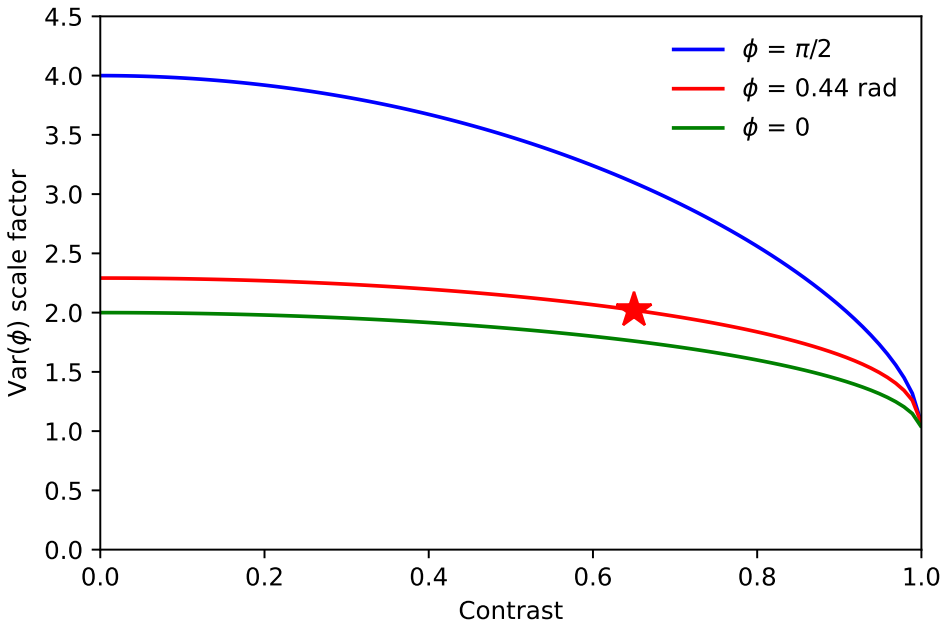

FIG. S 3. Additional scale factor for the variance of differential phase ϕ. The red star corresponds to the measurement of relative stability taken in the main text (Fig.3a) with $\phi = 0.44$ rad and $C = .65$.

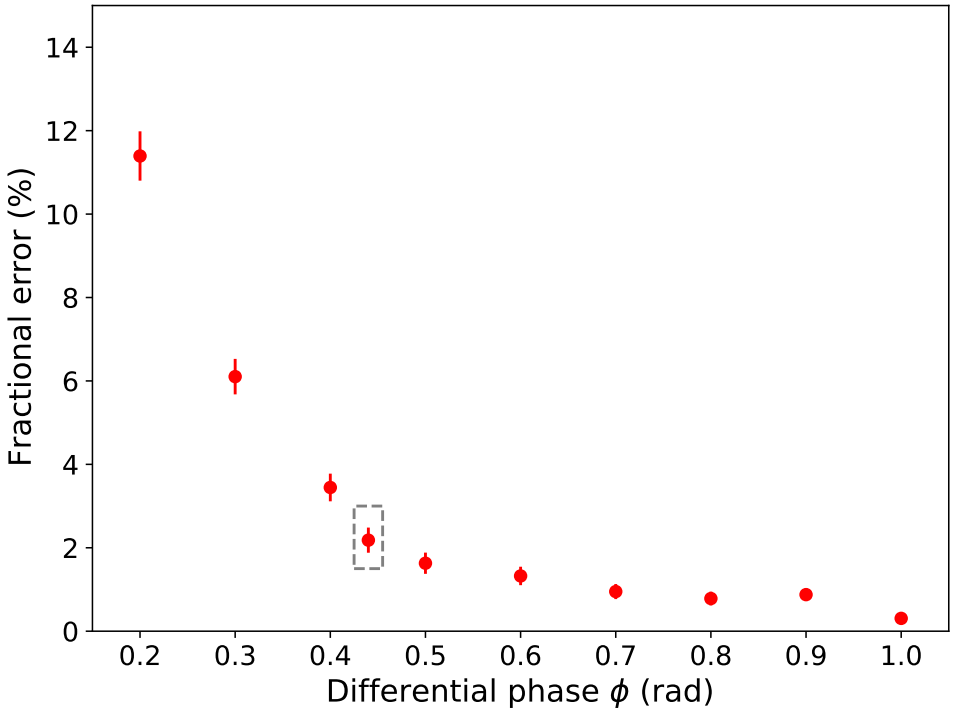

FIG. S 4. Monte-Carlo simulations of fractional biased error in ellipse fitting for 2400 atoms in each ensemble. The grey box corresponds to $\phi = 0.44$ rad, at which the biased error can be bound below 3%.

shows a simulated ellipse and its fitting at $\phi = 0$ rad with 500 atoms, 100 measurement runs and 0.65 contrast for each ensemble. The corresponding histograms for excitation fractions are shown on the top and right axes. Fig.S5b is the Monte-Carlo simulation at different contrasts

with the above parameters as input. The extracted contrast is slightly below the true contrast, and is accounted for by adding a small offset, typically below 0.02. We note that this approach depends on the sampling of ellipse, a typical number of 100 to 200 measurement runs is required to ensure the accuracy of the extracted contrast. For measurements with long interrogation time that don't have enough data points due to short total averaging time, i.e., Fig.2d (iii) in the main text, the difference between the maximum and minimum in excitation fractions is used to extract the contrast.

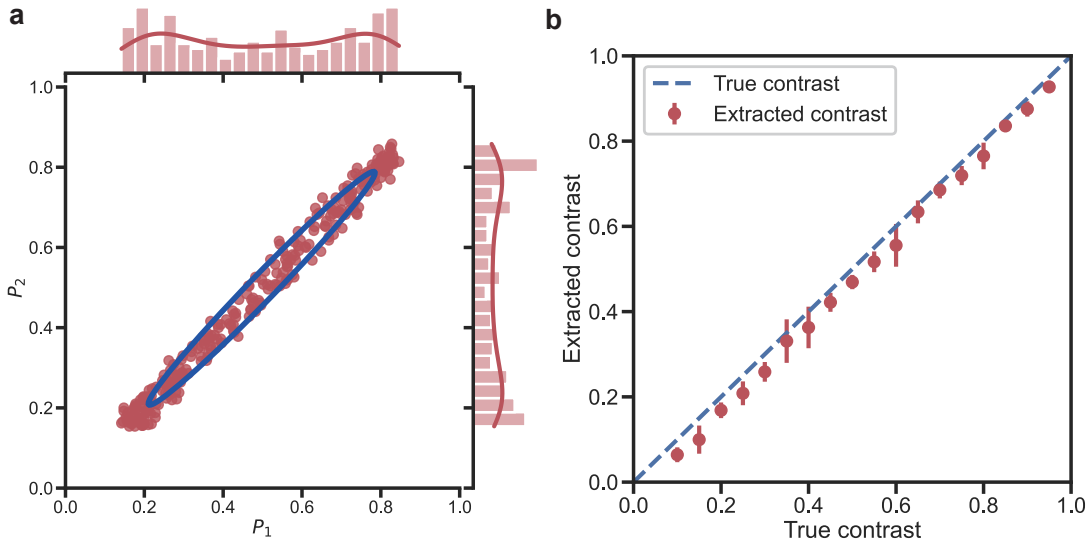

FIG. S 5. Contrast Monte-Carlo simulation. (a) Parametric and histogram plots showing contrast subtraction for simulated data at 0 rad offset phase with a contrast of 0.65, 500 atoms and 100 measurement runs as input. (b) Monte-Carlo simulation with an offset phase at 0 rad by varying the input contrast. The dashed line represents the case when the extracted contrast equals the true contrast, indicating that the subtracted contrast is slightly underestimated. The offset will then be used to correct the subtracted contrast.

F. Loading dual isotopes into the lattice

The experimental sequence for loading dual isotopes into the lattice is shown in Fig.S6. We first load ^{87}Sr into the lattice, and move the ensemble 1 cm away from the lattice beam waist. Unlike loading multiple ensembles of the same isotope, here we must perform a second round of cooling in the 461-nm and 689-nm MOTs to address the second bosonic isotope (^{88}Sr, ^{86}Sr or ^{84}Sr) due to isotope-dependent shifts in their energy levels. This requires shifting the frequencies of the 461-nm lasers, including the 2D-MOT, Zeeman slower, 3D-MOT and probe lasers, by as much as 270 MHz. The frequency gap is bridged by double-passing the master 461-nm laser through two AOMs [13] operating at 350 MHz with a bandwidth of about 150 MHz, and then subsequently used to injection lock three laser diodes which are sent to the experiment table. A simultaneous frequency tuning of up to 270 MHz within 100 ms can be achieved while maintaining the injection locking. To efficiently cycle the 461-nm MOT for all 4 isotopes, the two repumping lasers, operating at 679 nm ($^3P_0 \leftrightarrow {}^3S_1$) and 707 nm ($^3P_2 \leftrightarrow {}^3S_1$), are frequency modulated at 1 kHz with 1.5 GHz and 4 GHz amplitudes, respectively. For the 689 nm lasers, the frequencies need to be shifted by about 1.5 GHz. This is done by jumping the radio-frequency signal that is used to reference the optical offset phase lock. (We thank Vescent Photonics for offering us a discount on the Offset Phase Lock Servo D2-135 used to accomplish

this.) To avoid heating the ^{87}Sr samples out of the lattice during the loading of the second isotope, ^{87}Sr is coherently transferred and shelved in the $^3P_0$ state via a π-pulse and the 679 nm repump laser is disabled during the 461-nm MOT stage for the second isotope. A final lattice movement brings the two isotopes back to balanced separations from the lattice center, where two sets of imaging pulses with varying frequencies are used to image both isotopes separately.

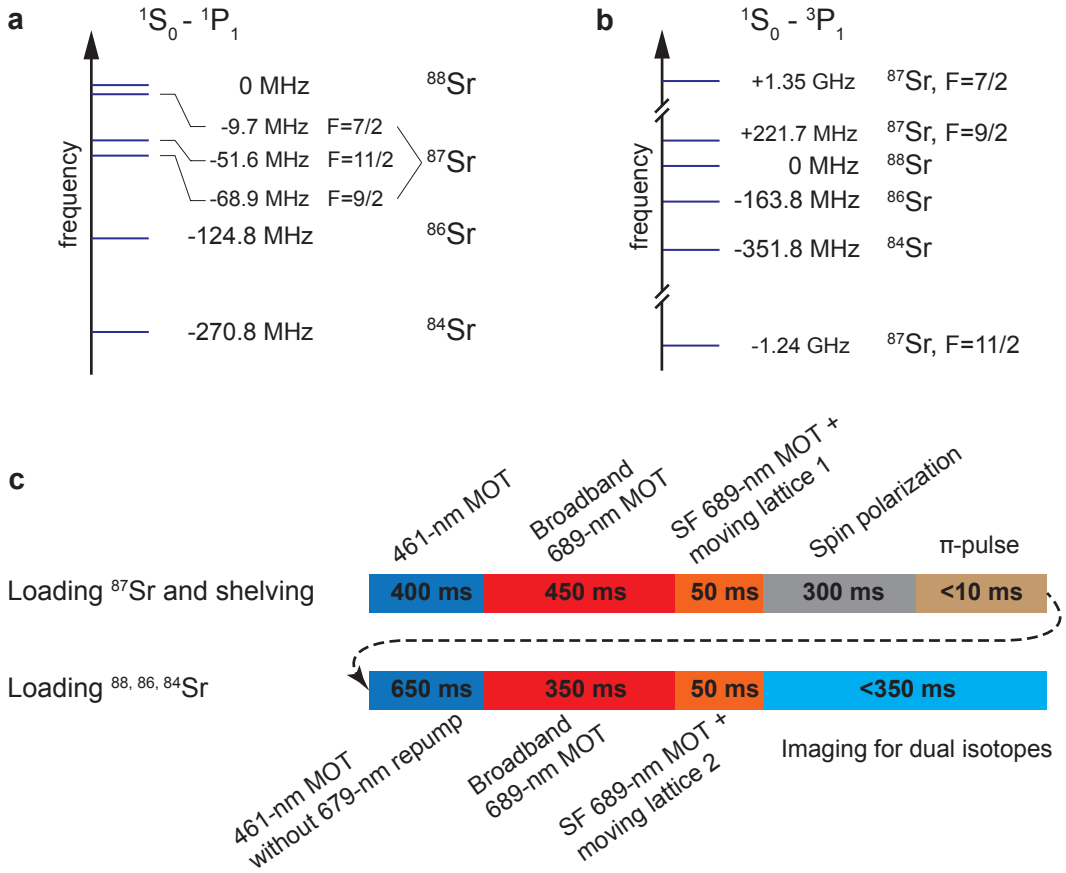

FIG. S 6. Loading dual isotopes. (a) Isotope shifts on the 461 nm $^1S_0 \leftrightarrow {}^1P_1$ transition for producing the first stage MOT. The isotope shifts are relative to resonance of ^{88}Sr. Note that for ^{87}Sr, the $F = 11/2$ transition is chosen to optimize the MOT. (b) Isotope shifts on the 689 nm $^1S_0 \leftrightarrow {}^3P_1$ transition for making the second stage MOT. For ^{87}Sr, both the $F = 9/2$ and $F = 11/2$ transitions addressed. (c) Timing diagram for loading dual isotopes into the lattice.

G. Six ensembles differential clock comparisons

1. Experimental sequence

To load 6 ensembles, we modify the loading sequence for one ensemble such that the maximal detuning of the retro-reflected lattice light is 2 MHz with 1 ms ramp time, corresponding to a maximal velocity of $\sim$0.8 m/s and acceleration of $\sim$81 g. This loading sequence is repeated 5 times, such that 5 subsets of the atomic ensembles can be separated from the original cloud with equal separations of 0.2 cm. The imaging pulse duration is kept below 250 μs to reduce cross-talk due to smaller separation between nearby ensembles.

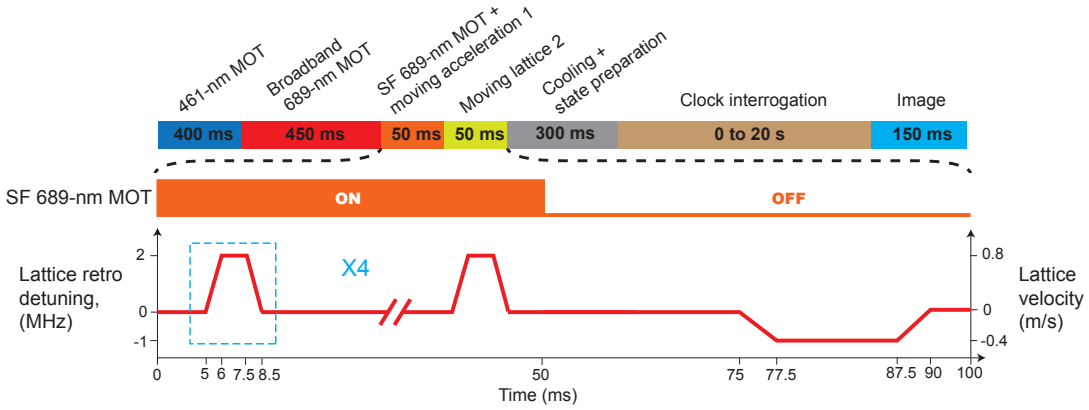

FIG. S 7. Timing diagram for loading 6 ensembles into the lattice.

2. Determination of differential frequencies

To determine the differential frequencies between each clock comparison, we run at different Ramsey times ranging from 2.5 to 8.5 s, and map out the differential frequency through the accumulated phase evolution, which follows

$$\phi_{\mathrm{acc},ij}(T) = 2\pi\delta f_{ij} T, \tag{19}$$

where T is the Ramsey interrogation time, and $\delta f_{ji} = f_j - f_i$ is the differential frequency between ensemble j and ensemble i. Note that $\delta f_{ij} = -\delta f_{ji}$. While this is not entirely correct due to the bias error from ellipse fitting, we perform Monte-Carlo simulations for each resulting pairwise ellipse using the contrasts and atom numbers extracted from each ensemble independently, and correct for the bias errors before mapping out the differential frequencies.

3. "Closed-loop" analysis

To verify that the 15 pairwise comparisons are self-consistent, we perform a "closed-loop" analysis in which each loop contains 3 or more "clocks". While the result of an individual pairwise comparison contains both differential frequencies and measurement noises, the sum of the differenial frequencies around a "closed-loop" should always be zero, leaving only measurement noise regardless of any spatial gradients or systematic shifts.

Since the sum frequencies after clockwise and anti-clockwise rotations are equivalent, the number of ways to arrange n "clocks" in a loop is $(n-1)!/2$. For example, consider a loop that has 6 "clocks", compared in the order $(1, 2, 3, 4, 5, 6)$. The resulting sum frequency can then be calculated as

$$f = \delta f_{21} + \delta f_{32} + \delta f_{43} + \delta f_{54} + \delta f_{65} - \delta f_{61}. \tag{20}$$

Note that this is equivalent to the sum frequencies of $(2, 3, 4, 5, 6, 1)$, $(3, 4, 5, 6, 1, 2)$, $(4, 5, 6, 1, 2, 3)$, $(5, 6, 1, 2, 3, 4)$ and $(6, 1, 2, 3, 4, 5, 6)$. Therefore, we have $5!/2 = 60$ unique combinations for loops of 6 "clocks". For loops of 5 "clocks", there are 6 choose 5 ($_6C_5$) combinations to choose 5 ensembles, and $4!/2 = 12$ ways to arrange the "clocks", resulting in a total of 72 combinations. Similarly, there are $_6C_4 \times 3!/2 = 45$ combinations for loops of 4 "clocks", and $_6C_3 \times 2!/2 = 20$ combinations for loops of 3 "clocks". Finally, this gives $60 + 72 + 45 + 20 = 197$ unique combinations for simultaneous clock comparisons of 6 ensembles.

H. Calibration of spatial gradient in fluorescence imaging

In order to ensure fidelity in our simultaneous measurements of excitation fractions in each region, we must calibrate the spatial gradient of our fluorescence imaging efficiency along the lattice. This gradient mainly arises from the spatial inhomogeneity of fluorescence collection and the imaging beam intensity gradient, as well as pixel by pixel variation of quantum efficiency across the camera's electron multiplying charge-coupled device (EMCCD). To calibrate our spatial imaging efficiency, an ensemble of atoms is loaded into the lattice and moved at a constant velocity of 1.5 m/s and is imaged along the lattice over 500 camera pixels, corresponding to a distance of approximately 1.5 cm. This is carried out within 100 ms, with a moving velocity chosen to ensure atom loss is negligible over this time scale, which is much smaller than the ground state atom lifetime (> 20 s). A Gaussian fit to the trace of the atomic cloud gives the amplitude and center of the cloud in units of pixel index number. An average of 10 repeated measurements are taken to map out the imaging gradient. A Savitzky-Golay filter is then applied to smooth out the normalized imaging efficiency curve [14], which is used to post-calibrate our data from a raw EMCCD fluorescence image. A typical calibration curve with 10 averages is shown in Fig.S8.

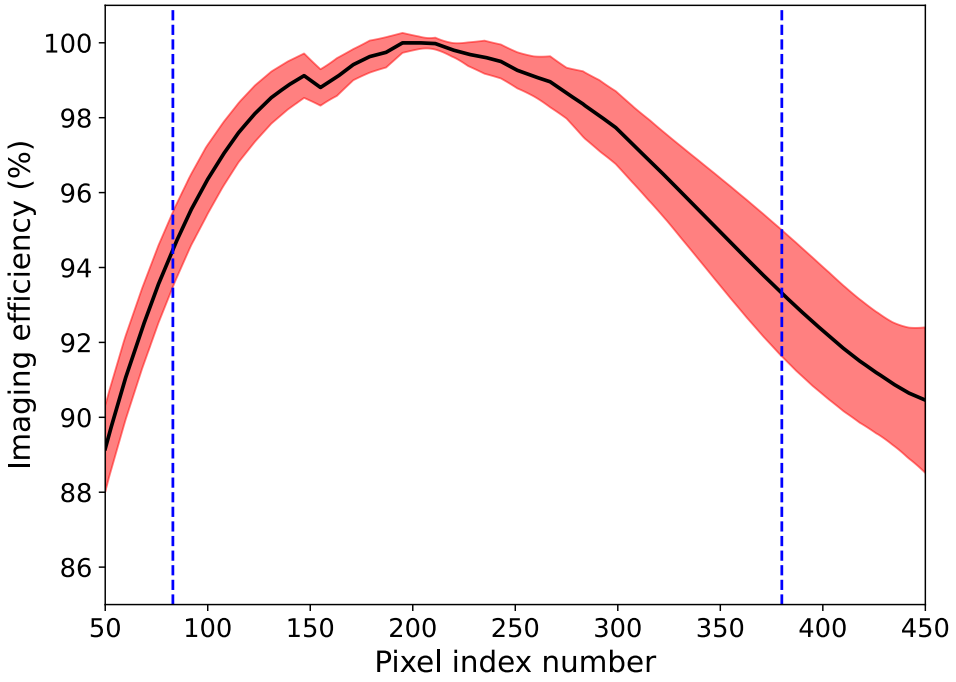

FIG. S 8. Calibration of fluorescence imaging gradient along the lattice. The black line is the averaged normalized imaging efficiency, the red area indicates the corresponding 1σ standard error. The blue dashed lines represent the pixel indices (along the gravitational axis, $\hat{z}$) at which two ensembles are separated by 1 cm.

References

[1] S. Blatt et al. Rabi spectroscopy and excitation inhomogeneity in a one-dimensional optical lattice clock. *Phys. Rev. A* **80**, 052703 (2009).

[2] S. Dörscher et al. Lattice-induced photon scattering in an optical lattice clock. *Phys. Rev. A* **97**, 063419 (2018).

[3] T. Bothwell et al. JILA SrI optical lattice clock with uncertainty of 2.0×10^{-18}. *Metrologia* **56**, 065004 (2019).

[4] M. M. Boyd. High precision spectroscopy of strontium in an optical lattice: towards a new standard for frequency and time. *Ph.D. thesis* (2007).

[5] P. G. Westergaard et al. Lattice-induced frequency shifts in Sr optical lattice clocks at the 10^{-17} level. *Phys. Rev. Lett.* **106**, 210801 (2011).

[6] I. Ushijima, M. Takamoto, and H. Katori. Operational magic intensity for Sr optical lattice clocks. *Phys. Rev. Lett.* **121**, 263202 (2018).

[7] R. C. Brown et al. Hyperpolarizability and operational magic wavelength in an optical lattice clock. *Phys. Rev. Lett.* **119**, 253001 (2017).

[8] T. L. Nicholson et al. Systematic evaluation of an atomic clock at 2×10^{-18} total uncertainty. *Nat. Commun.* **6**, 6896 (2015).

[9] M. M. Boyd et al. Nuclear spin effects in optical lattice clocks. *Phys. Rev. A* **76**, 022510 (2007).

[10] G. E. Marti et al. Imaging optical frequencies with 100 μHz precision and 1.1 μm resolution. *Phys. Rev. Lett.* **120**, 103201 (2018).

[11] A. W. Young et al. Half-minute-scale atomic coherence and high relative stability in a tweezer clock. *Nature* **588**, 408–413 (2020).

[12] R. Halir and J. Flusser. Numerically stable direct least squares fitting of elllipses. *Proc. of Sixth Intl Conf. Computer Graphics and Visualization* **1** (1998).

[13] S. Stellmer. Degenerate quantum gases of strontium. *Ph.D. thesis* (2014).

[14] A. Savitzky and M. J. E. Golay. Smoothing and differentiation of data by simplified least squares procedures. *Analytical Chemistry* **36**, 1627-1639 (1964).